



Estimating high frequency energy radiation of large earthquakes by image deconvolution back-projection



Dun Wang^{a,*}, Nozomu Takeuchi^a, Hitoshi Kawakatsu^a, Jim Mori^b

^a Earthquake Research Institute, University of Tokyo, 1-1-1, Yayoi, Bunkyo-ku, Tokyo, 113-0032, Japan

^b Disaster Prevention Research Institute, Kyoto University, Uji, Kyoto 611-0011, Japan

ARTICLE INFO

Article history:

Received 3 February 2016

Received in revised form 27 May 2016

Accepted 28 May 2016

Available online 9 June 2016

Editor: P. Shearer

Keywords:

back-projection
seismic array
high frequency energy radiation
rupture speed
supershear

ABSTRACT

High frequency energy radiation of large earthquakes is a key to evaluating shaking damage and is an important source characteristic for understanding rupture dynamics. We developed a new inversion method, Image Deconvolution Back-Projection (IDBP) to retrieve high frequency energy radiation of seismic sources by linear inversion of observed images from a back-projection approach. The observed back-projection image for multiple sources is considered as a convolution of the image of the true radiated energy and the array response for a point source. The array response that spreads energy both in space and time is evaluated by using data of a smaller reference earthquake that can be assumed to be a point source. The synthetic test of the method shows that the spatial and temporal resolution of the source is much better than that for the conventional back-projection method. We applied this new method to the 2001 M_w 7.8 Kunlun earthquake using data recorded by Hi-net in Japan. The new method resolves a sharp image of the high frequency energy radiation with a significant portion of supershear rupture.

© 2016 Elsevier B.V. All rights reserved.

1. Introduction

With the recent establishment of regional dense seismic arrays (e.g., Hi-net in Japan, USArray in the North America), advanced digital data processing has enabled improvement of back-projection methods that have become popular and are widely used to track the rupture process of moderate to large earthquakes (e.g. Ishii et al., 2005; Krüger and Ohrnberger, 2005; Vallée et al., 2008; Walker and Shearer, 2009; Honda et al., 2011; Meng et al., 2011; Wang and Mori, 2011; Koper et al., 2012; Yagi et al., 2012; Yao et al., 2012; Kennett et al., 2014).

For all of these studies, time differences among seismograms recorded across regional or global arrays are used to trace the rupture migration. The methods can be classified into two groups, one using time domain analyses (Ishii et al., 2005; Krüger and Ohrnberger, 2005; Vallée et al., 2008; Walker and Shearer, 2009; Honda et al., 2011; Wang and Mori, 2011; Koper et al., 2012; Yagi et al., 2012; Yao et al., 2012), and the other frequency domain analyses (Meng et al., 2011; Yao et al., 2013). There are

minor technique differences in both groups, such as the stacking methods (linear stacking, Nth-root stacking, for example, Xu et al., 2009), and the usage of cross correlation coefficients instead of stacking amplitudes (Ishii, 2011; Yagi et al., 2012). Surprisingly, all the aforementioned methods usually give consistent results, if the same datasets are used, which has been verified by the images for the March 11, 2011 Tohoku, Japan M_w 9.0 earthquake.

Here we focus on the back-projection performed in the time domain using seismic waveforms recorded at teleseismic distances (30°–90°). For the standard back-projection (Ishii et al., 2005), teleseismic P waves that are recorded on vertical components of a dense seismic array are analyzed. Since seismic arrays have limited resolutions and we make several assumptions (e.g., only direct P waves at the observed waveforms, and every trace has completely identical waveform), the final images from back-projections show the stacked amplitudes (or correlation coefficients) that are often smeared in both time and space domains. Although it might not be a serious issue to reveal overall source processes for a giant seismic source such as the 2004 M_w 9.0 Sumatra earthquake where the source extent is about 1400 km (Ishii et al., 2005; Krüger and Ohrnberger, 2005), it becomes a severe problem to image detailed processes of earthquakes with smaller source dimensions, such as a M_w 7.5 earthquake with a source extent of 100–150 km. For smaller earthquakes, it is more difficult to resolve space distributions of the radiated energies. For the 2009 M_w 6.3

* Corresponding author.

E-mail address: dunwang@eri.u-tokyo.ac.jp (D. Wang).

¹ Present address: State Key Laboratory of Geological Processes and Mineral Resources, School of Earth Sciences, China University of Geosciences, Wuhan 430074, China.

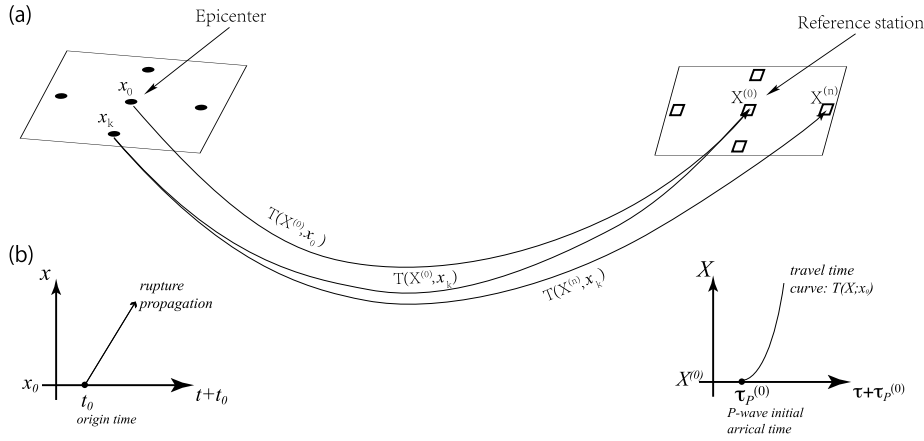


Fig. 1. Schematic illustrations of (a) the ray paths from the source grids to the seismic stations, and (b) the difference of time and space coordinates in source and station domains.

L'Aquila, Italy earthquake, the area of the cumulative energy shows an elliptical shape centered at the epicenter due to the large effects of the array smear (D'Amico et al., 2010).

There have been a few studies that try to improve resolution by taking the special resolution kernel (or spatial smearing) into account (Lay et al., 2009; Wang et al., 2012; Haney, 2014; He et al., 2015; Nakahara and Haney, 2015). Wang et al. (2012) deconvolved array spatial smearing that is evaluated by using the back-projection image of an aftershock, to improve the spatial resolution. Since the deconvolution was done individually for each time window, the temporal resolution was not improved. Similar ideas have been implemented for improving the spatial resolution of monitoring volcanic tremors (Haney, 2014).

In this work, we extend the idea of Wang et al. (2012) by considering the smearing both in space and time domains. It is evaluated by the spatial and temporal distribution of the back-projected image for a small earthquake that can be assumed as a point source. In this approach, the contributions of later phases (i.e. depth phases) can be taken into account, which is one of the advantages of the method in this study. Therefore this method obtains the true energy radiation of the ruptured fault, minimizing/excluding propagation effects from structures in the earth, for example, depth phases from the Earth's free surface.

2. Method: image deconvolution back-projection

In this study, we introduce a new inversion method, Image Deconvolution Back-Projection (IDBP), to refine the source image obtained by the sliding-window beampacking of Wang et al. (2016), which is similar to Krüger and Ohrnberger (2005). However, as our new method is applicable to more general back-projection approaches (e.g., Ishii et al., 2005), we first summarize both the conventional back projection and the sliding-window beampacking methods.

2.1. Conventional imaging methods

In the conventional back projection (BP), the stacked power, $\Psi^{BP}(x, t)$ for the source location x and time t is evaluated by

$$\Psi^{BP}(x, t) = \frac{1}{N} \int_{t-\Delta t/2}^{t+\Delta t/2} \left\{ \sum_n v(X^{(n)}, t' + t_0 + T(X^{(n)}; x)) \right\}^2 dt', \quad (1)$$

where v is a certain component seismogram, $X^{(n)}$ is the location of the n -th station. t_0 is the origin time, and $T(X^{(n)}; x)$ is the travel time from the source location x to the station location $X^{(n)}$, Δt is the width of the time window, and N is the number of stations.

In the sliding-window beampacking, the stacked array beam power (AP), $\Psi^{AP}(x, \tau)$ is evaluated by

$$\Psi^{AP}(x, \tau) = \frac{1}{N} \int_{\tau-\Delta\tau/2}^{\tau+\Delta\tau/2} \left\{ \sum_n v(X^{(n)}, \tau' + \tau_p^{(0)} + T(X^{(n)}; x) - T(X^{(0)}; x)) \right\}^2 d\tau' \quad (2)$$

where $X^{(0)}$ is the location of the reference station, and $\tau_p^{(0)}$ is the arrival time of the initial P-phase at the reference station. A P-wave that arrives at the time $\tau + \tau_p^{(0)}$ to the reference station should arrive to a station at X at time $\tau_p(X) = \tau + \tau_p^{(0)} + T(X; x) - T(X^{(0)}; x)$ if the energy is radiated from a source point x . Fig. 1 illustrates the ray paths for travel times $T(X^{(0)}; x_0)$, $T(X^{(0)}; x_k)$, and $T(X^{(n)}; x_k)$, as well as the coordinate system employed here: in the source side, x_0 and x_k denote locations of the epicenter and k -th subevent, respectively, and in the array side, $X^{(0)}$ and $X^{(n)}$ denote locations of the reference and n -th stations, respectively; the superscript (n) generally denotes the station coordinate. In equation (2), we stack the waveform along that travel time curve to enhance the signal only when the energy indeed came from that source point. Note that the meaning of t for $\Psi^{BP}(x, t)$ and τ for $\Psi^{AP}(x, \tau)$ are different, so we use different notations; the former is the source time relative to the origin time, while the latter is the P arrival time relative to the onset time in the waveform of the reference station (Fig. 1(b)). We therefore need a correction to transform τ to t using the following relation:

$$t(x, \tau) = \tau + \tau_p^{(0)} - t_0 - T(X^{(0)}; x). \quad (3)$$

Hereafter we refer to this correction as “time correction”. It can be also expressed as

$$\tau(x, t) = t + t_0 + T(X^{(0)}; x) - \tau_p^{(0)}. \quad (3')$$

Both of $\Psi^{BP}(x, t)$ and $\Psi^{AP}(x, \tau)$ with the time correction give similar image of the source energy radiation, and as we can see in equations (1), (2) and (3), two methods are equivalent.

In computing the image $\Psi^{AP}(x, \tau)$ by using eq. (2), we need to evaluate the following travel time:

$$\tau_p^{(0)} + [T(X^{(n)}; x) - T(X^{(0)}; x)]. \quad (4)$$

In this study, the arrival time $\tau_p^{(0)}$ is manually picked from the onset time of the first P pulse at the reference station. In evaluating the differential travel time within the square braces, we take the

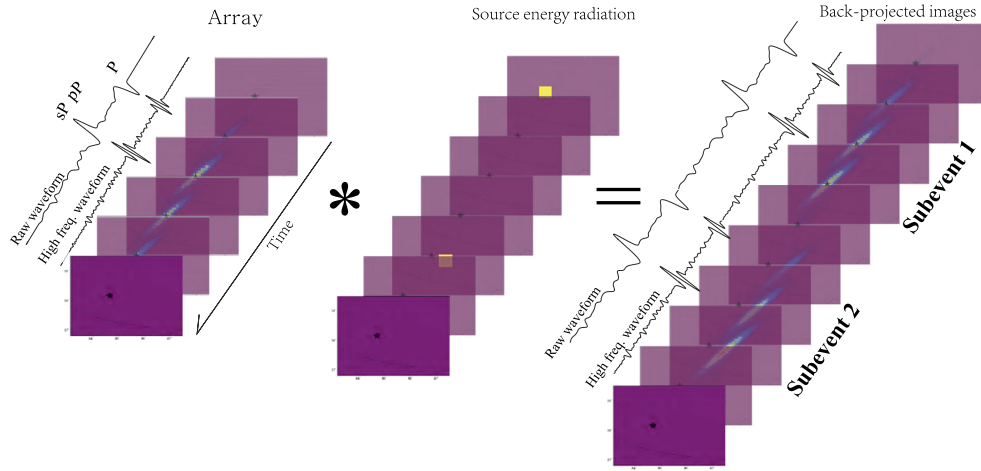


Fig. 2. Diagram showing the idea of the new approach. The array stacked images of a large earthquake (right hand side) can be thought of as the temporal and spatial convolution of an array response (left most) and the source distribution (middle). The array response can be determined using the stack amplitudes of a moderate earthquake, which is assumed to be a point source in time and space.

station correction into account. We compare the synthetic differential travel time for $[T(X^{(n)}; x_0) - T(X^{(0)}; x_0)]$ to the observed differential travel time, $\tau_p^{(n)} - \tau_p^{(0)}$, (where $\tau_p^{(n)}$ is the arrival time at the n -th station), evaluated by using the cross correlation of the first 6 sec of the P waveforms of the n -th and the reference station. Assuming the effect of the unmodeled 3D structure is mostly shared by similarity of the teleseismic ray paths, we attribute the residuals between two differential travel time to a station term and add it to the synthetic differential travel time for $[T(X^{(n)}; x) - T(X^{(0)}; x)]$.

2.2. Image deconvolution

Fig. 2 illustrates how the back-projection image is related to the source radiation energy and the array response. As for the array response, we use the image, either $\Psi_m^{BP}(x, t)$ or $\Psi_m^{AP}(x, \tau)$, for a reference event that has a smaller fault area with a similar radiation pattern as that of the mainshock. We assume that the reference event has the moment density tensor $m_{pq}(x, t)$ and is well approximated by a point source. We define its centroid time and location as $t = 0$ and $x = 0$, respectively. $\Psi_m^{BP}(x, t)$ or $\Psi_m^{AP}(x, \tau)$ should have larger absolute values only when t (or τ) and x are both close to zero. However, the function actually has severe smearing owing to the limited resolution inherent from the array response and contamination by depth phases in time.

For the mainshock with the moment density tensor M_{pq} , we assume that the source can be expressed by appropriate superposition of the reference earthquake:

$$M_{pq}(x, t) \approx \sum_k A_k m_{pq}(x - x_k, t - t_k), \quad (5)$$

where x_k and t_k denote the centroid location and time of the k -th subevent, respectively, and A_k is the amplifying parameter for the k -th subevent (here we assume that the epicenter x_0 can be treated as a centroid). We assume $A_k \geq 0$. Under assumptions detailed in the Supplementary material (e.g., incoherency of waveforms generated by subevents at high-frequencies; equation (S3)), the conventional back-projection image $\Psi^{BP}(x, t)$ should have the following relations to that for the reference event:

$$\Psi^{BP}(x, t) \approx \sum_k A_k^2 \Psi_m^{BP}(x - x_k, t - t_k). \quad (6)$$

Using this equation, we invert $\Psi^{BP}(x, t)$ for A_k^2 by applying the non-negative least square method (Lawson and Hanson, 1974). The obtained A_k^2 , x_k and t_k values offer sharp source images.

In a similar fashion, we can refine the image of the mainshock obtained by the sliding-window beampacking method, $\Psi^{AP}(x, \tau)$, by using the image for the reference event $\Psi_m^{AP}(x, \tau)$. We first invert for A_k^2 by using

$$\Psi^{AP}(x, \tau) \approx \sum_k A_k^2 \Psi_m^{AP}(x - x_k, \tau - \tau_k), \quad (7)$$

where $\tau_k = \tau(x_k, t_k)$ is the arrival time of the k -th subevent to the reference station. We next apply time correction and interpret that they are the energy radiation at $t = t(x_k, \tau_k)$. In the example shown later, we solve eq. (7) rather than (6). The inversion greatly refines the source image, which we will show in the next section. As the method is based on the deconvolution of the image obtained by back-projection, we name it as Image Deconvolution Back-Projection (IDBP).

3. Numerical test

We perform a numerical test to evaluate the resolution of the new approach for determining rupture location and time. We generate synthetic waveforms for the geometry of the 2001 M_w 7.8 Kunlun, China earthquake recorded by the Hi-net array in Japan. Hi-net consists of ~ 770 stations (operated by the National Research Institute for Earth Science and Disaster Prevention, Okada et al., 2004), which are located at azimuths of 52° to 72° , and at distances of 38° to 50° from the event (Fig. 3).

Synthetic seismograms including seismic phases P, pP, and sP are calculated using the method of Kikuchi and Kanamori (<http://www.eri.u-tokyo.ac.jp/ETAL/KIKUCHI/>, 2006). The source model consists of six point sources with equal seismic moments that are horizontally spaced at a 45 km interval along the fault line with a strike-slip focal mechanism (strike = 94° , dip = 61° , slip = -12°) at a depth of 10 km. A triangle shaped source time function with a half width of 1 s and seismic moment of 1×10^{18} Nm is set for each point source. The sampling interval is 0.01 s, the same as that of the Hi-net data. The source starts from the epicenter (90.541°E , 35.946°N , determined by USGS), and extends eastward with a rupture speed of 3.5 km/s.

We add ambient noise for a typical early morning period (2013/11/15 05:25:00 to 2013/11/15 05:34:59 JST) to the synthetic waveform at each station. The noise is band-pass (1.0 to 10.0 Hz) filtered, and added to the synthetic waveforms computed for the scenario described above. The level of the noise is adjusted so that the signal (synthetic) to noise ratio is 10, which is comparable to the data recorded for the Kunlun earthquake.

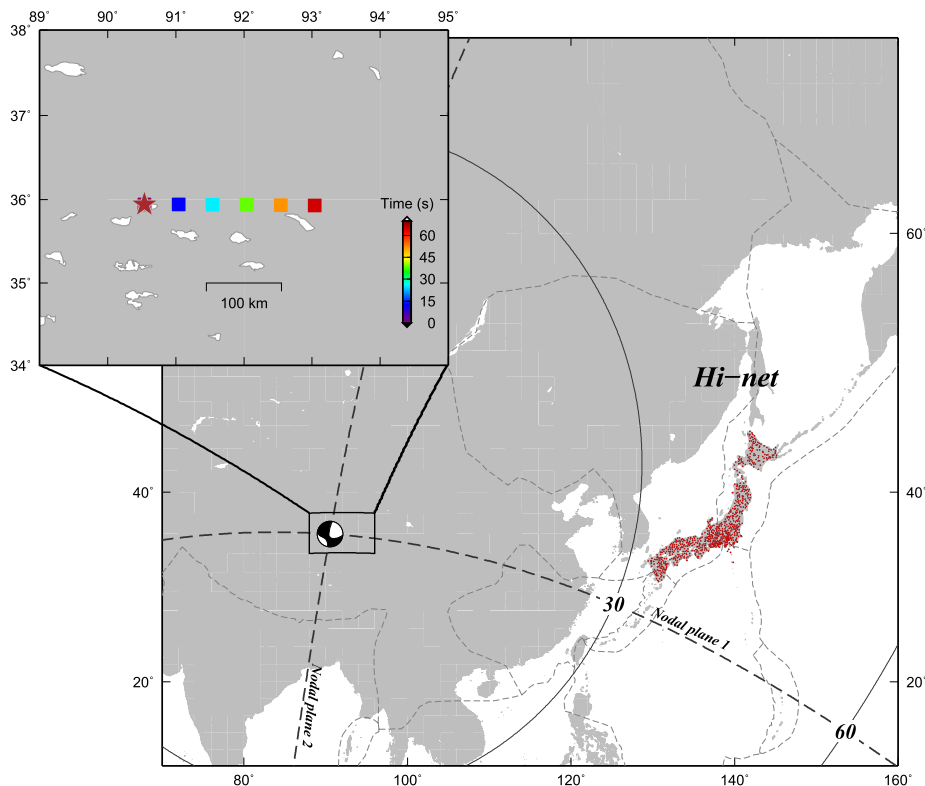


Fig. 3. Geometry of the stations in Hi-net with respect to the epicenter of the 2001 M_w 7.8 Kunlun earthquake. Top inset shows the input model for generating synthetic waveforms in the synthetic test. The focal mechanism of the input model is the same as for the earthquake obtained from the Global CMT Project.

We set up a 41×41 spatial grid with points evenly spaced by 15 km interval on a horizontal plane at depth 10 km. Similar to the procedure used in the standard back-projection approach, we align the first 6 s of the waveforms to measure differential travel time $\tau_p^{(n)} - \tau_p^{(0)}$, and the sliding-window beampacking procedure is carried out on the waveforms, with window length ($\Delta\tau$) of 6 s.

For the image of the reference event, we generate waveforms for a point source that is located at the epicenter of the 2001 Kunlun earthquake and has the same focal mechanism as the model for the six point sources, and then conduct sliding-window beampacking to the waveforms. To obtain the images, we set up a larger horizontal grid system that consists of 121×121 points with the same space interval. This is because, in eq. (7), we need quantities of $\Psi_m^{AP}(x - x_k, \tau - \tau_k)$ for larger $|x - x_k|$ (e.g., for the case when x and x_k are located in the eastern and the western end of the tested grid point of the source). As for the temporal grids, we set a time interval of 2 s.

In the inversion procedure, we assume that, for each time step, energy is radiated from regions where a sliding-window beampacking produces amplitudes that are larger than 80% of the maximum amplitude at each time step. This reduces the size of the matrix in the inversion, therefore significantly reducing the computation time for the inversion. It also helps to stabilize inversion of the matrix and effectively acts as a regularization. As for real data, the number of subevents, k , and the grid size are determined by the aftershock distribution and results of previous studies.

Fig. 4 shows the comparison between the energy distribution in time and space derived from the standard imaging method and the new method we propose. The standard method, due to the array response and the finite length of the stacking window, produces a large smear in the image both in time and space (Fig. 4b) that obscures identification of individual point sources. The new method resolves this problem, thus offering a sharp image for the rupture migration and energy radiation. For the results de-

rived from the new method, not only the rupture pattern and the rupture speed, but also the spatial and temporal locations of the individual sources are recovered very well, although there seems to be slightly larger distortion for the last subevent, probably due to the effect of the noise or slight inversion instability. We generate synthetic waveforms for subevents with varying depths (10, 12, 8, 15, 5, and 11 km), and image the source from the synthetic waveforms. The rupture speed and energy distribution are generally recovered (Fig. S1), although the resolution is not as good as for the constant focal depth scenario.

4. 14 October 2001 M_w 7.8 Kunlun earthquake

On 14 October 2001, a M_w 7.8 earthquake occurred along the Kunlun strike-slip fault, which is one of the major collisional strike-slip faults in the Tibetan Plateau (Fig. 5). Past geological, seismological, and geodetic studies have suggested that this earthquake ruptured over a length of nearly 400 km, with peak slip as large as 8 m (Xu et al., 2006). The source process of this earthquake has been extensively studied (Bouchon and Vallee, 2003; Lin et al., 2003; Antolik et al., 2004; Ozacar and Beck, 2004; Robinson et al., 2006; Vallée et al., 2008; Walker and Shearer, 2009), and thus it offers a good test case to see how the new method recovers the source details.

4.1. Data and analyses

We use vertical component records from Hi-net, Japan. For the imaging of the mainshock, we set a 41×41 grid points (spaced at 15 km, at a depth of 10 km) on a horizontal plane covering the source region inferred from the aftershock distribution. We choose a M_w 5.8 earthquake that occurred 120 km southwest of the epicenter (07 July 2003, 06:55:54, M_w 5.8, 89.47E, 34.61N, depth 17 km) as a reference earthquake. For the sliding-window beampacking of the reference earthquake, we set a larger horizontal grid

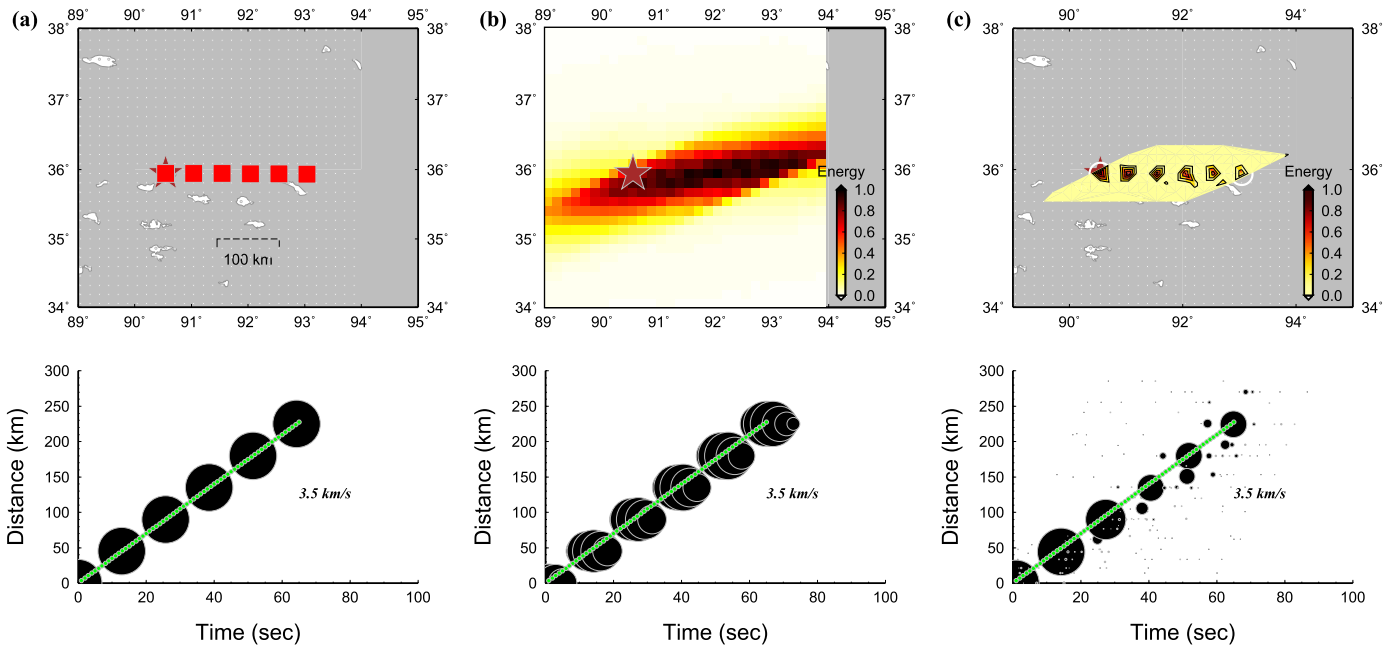


Fig. 4. (a): Top and bottom show the assumed point source locations and rupture speeds (3.5 km/s), respectively. The green line indicates a rupture speed of 3.5 km/s for reference. Star shows the epicenter of the initial point of the rupture. (b): Top shows cumulative radiated energies from the standard back-projection analyses using synthetic waveforms generated by the assumed point sources shown in (a). Bottom shows the time-distance plot of the maximum amplitude points. (c): Same as (b) for the new inversion method. (For interpretation of the references to color in this figure legend, the reader is referred to the web version of this article.)

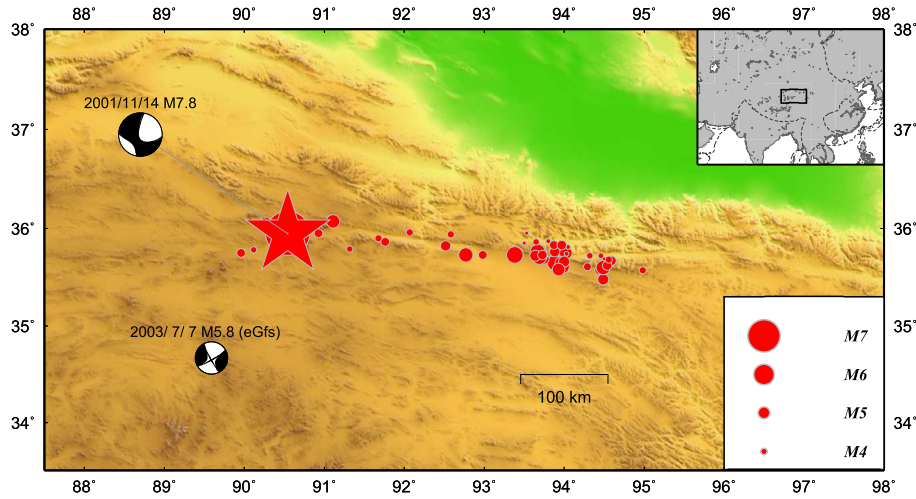


Fig. 5. Locations of aftershocks that occurred three months following the 2001 M_w 7.8 Kunlun earthquake. The red star indicates the epicenter of the earthquake (USGS). The focal mechanisms are from the Global CMT Project.

system of 121×121 points with the same spacing and strike as for the mainshock so that the mainshock rupture area can be well modeled.

Before imaging the source, we conduct appropriate pre-processing. The data are filtered using 2-pole Butterworth filters with corner frequencies at 1.0 and 10.0 Hz. We use the first 6 seconds of the P waveform of the reference station located in the vicinity of the centroid of the array as the reference seismogram, and those from individual stations that are not similar to the reference waveform are eliminated. This is done by evaluating the cross correlations of the first several seconds (6 s for the case of this study, the coefficient threshold is 0.4) of the P waves for each station with the reference seismogram. This procedure eliminates data that have strong site response or possible instrumental problems. We only use the stations that are located at distances between 30 and 90 degrees from the earthquake to minimize the effects of triplication and interference of other phases.

For the mainshock, station corrections are determined using cross correlations to align the first 6 s of all the data on the initial arrival. The same station corrections are then applied to the reference earthquake. The locations of the grid points are defined relative to the fixed epicenter determined by the USGS. Other parameters are the same as used in the synthetic test. Similar to the synthetic test, we reduce the dimensions of the matrix of the inversion. We pick spatial grid points whose amplitudes are larger than 80% of the maximum amplitude at each time step. These points are then set as the potential source locations in the inversion (blue colored area in Fig. 6).

4.2. Results

The inversion results for the Kunlun earthquake show sources of high frequency energy radiation with a clear eastward propagation. Fig. 6 shows the snap shots for the rupture propagation with

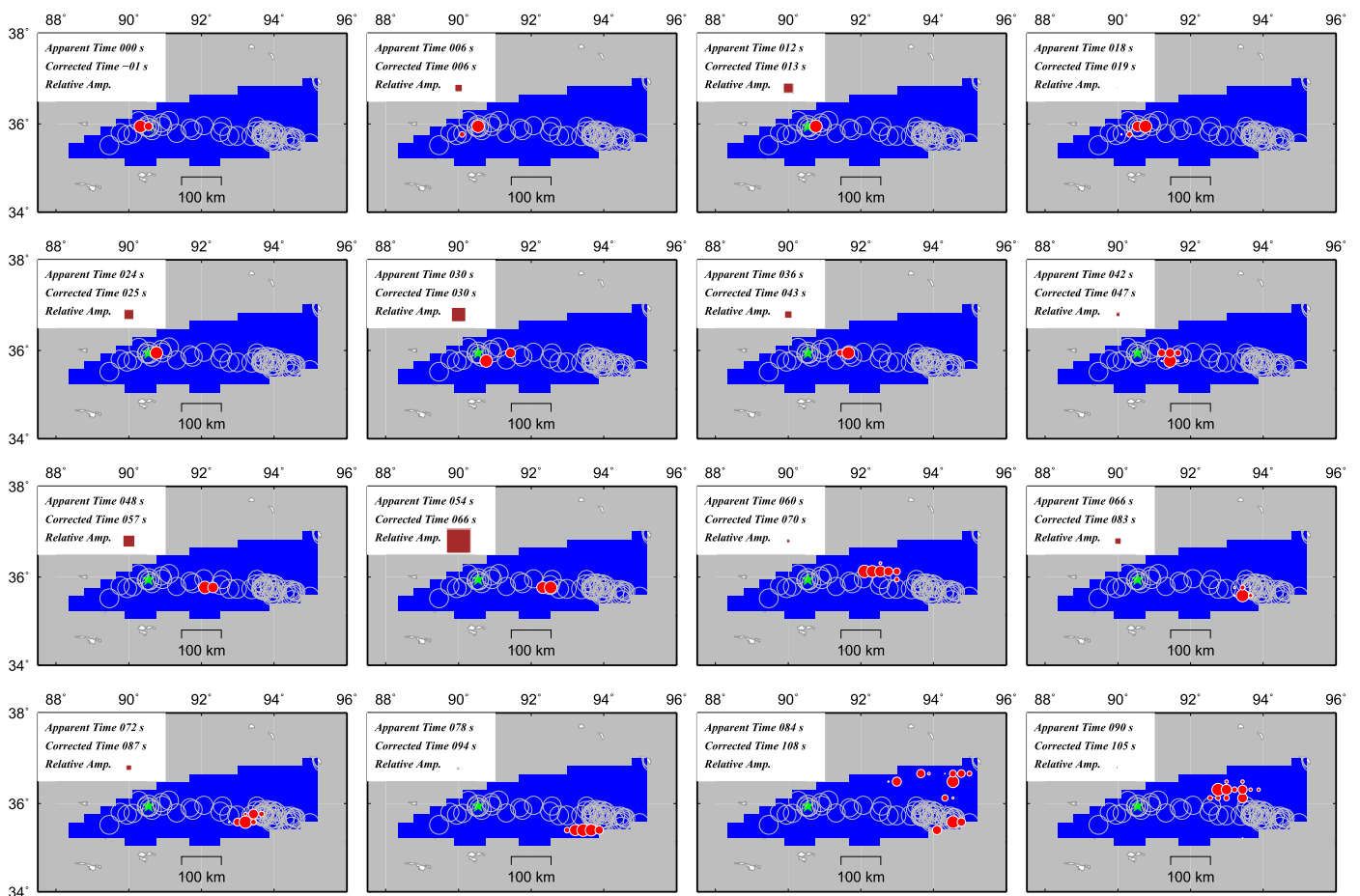


Fig. 6. Snap shots of the rupture propagation in ~ 6 s windows. Red circles show the location and amplitude (size of the circle) of the energy release. Blue area encloses points that are used as potential sources in inversion. Gray circles represent locations of aftershocks. Inset shows the timing and relative amplitude of the energy release with respect to the maximum energy release; apparent and corrected times respectively refer to τ and t in equations (2) and (1). (For interpretation of the references to color in this figure legend, the reader is referred to the web version of this article.)

a time interval of ~ 6 s. For the first 10–15 s, the rupture mainly propagates around the epicenter and slightly westward from the epicenter to a distance of ~ 40 km. This is consistent with the west surface slips that were reported by field investigations (Lin et al., 2003). Then the rupture migrates eastward along the Kunlun fault for ~ 360 km with a duration of 90 to 100 s. 110 s after the origin time, the radiated energy release ratio drops to 10% of the maximum. The total rupture length is 400 to 450 km. Comparing the locations of the energy radiation to the aftershock locations we infer that a good location resolution for the seismic sources are obtained.

The accumulated energy over the source process shows three clear peaks in time, suggesting three high frequency bursts (Fig. 7(b)), which are generally correlated with the source time function obtained by teleseismic waveform inversion (e.g., Robinson et al., 2006).

One interesting aspect of this event is the rupture speed. There is some debate if the rupture speed was faster than local shear wave velocity (supershear). For example, an analysis of surface waves recorded at regional broadband stations suggests that the average rupture speed was 3.7 to 3.9 km/s, with highest speed of 5.0 km/s along some segments (Bouchon and Vallee, 2003). Considering the possible depth variation for the rupture front, the obtained rupture speed gives the minimum of the true rupture speed. This observation is further supported by back-projections using a regional seismic array in Nepal (Vallée et al., 2008), and global data (Walker and Shearer, 2009). Considering that the local shear wave velocity is ~ 3.5 km/s at depths of 10 to 15 km (Laske et al., 2001),

the rupture might have been supershear. On the other hand, finite fault inversions using teleseismic waveforms suggest that the rupture speed was 3.4 to 3.6 km/s (Lin et al., 2003; Antolik et al., 2004; Ozacar and Beck, 2004) that is inconclusive for indicating a supershear rupture.

In this work, we observe a complex initiation; the rupture seems to propagate relatively slow and westward (or bilaterally) for the initial stage (first 15–20 s), and then expands eastward with a fast rupture speed of 4–5 km/s (Fig. 7(c)). If we estimate an overall average rupture speed from the onset time and the epicenter, the value is ~ 3.6 km/s, which generally agrees with the value obtained by the finite fault inversions (Lin et al., 2003; Antolik et al., 2004; Ozacar and Beck, 2004). This example suggests that there might be large variations for the rupture speed for some large earthquakes.

Comparison of the cumulative energy distributions derived from our new approach and the standard back-projection method indicates a much improved spatial resolution for this method. The stacked energy derived from the standard back-projection method is mainly masked by the array smear, although the maximum energy located to the east of the epicenter can be seen (Fig. 8(b)). The result derived from the new method clearly shows the details with the rupture extending eastward with three sources of high frequency energy radiation from 20 to 300 km east of the epicenter and ending in the area where most intense aftershock activity occurred. Among the three sources of high frequency radiation, the strongest burst was located close to the area with peak surface slip (Lin et al., 2003; Xu et al., 2006).

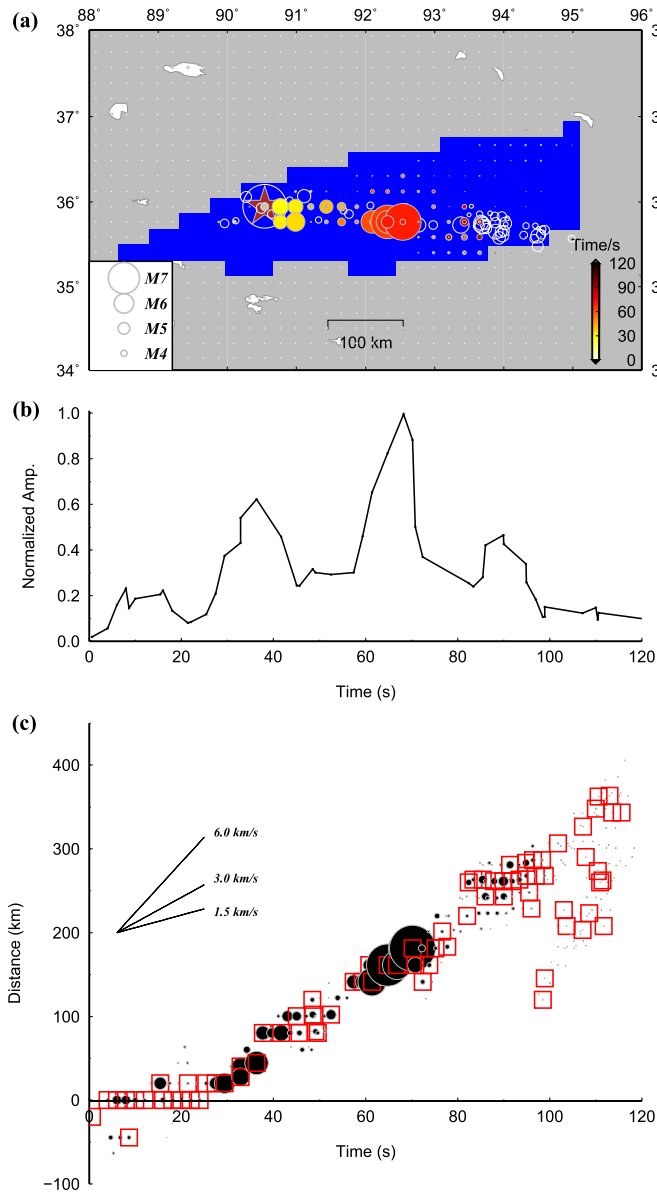


Fig. 7. (a): Image of the energy radiation for the November 14, 2001 M_w 7.8 Kunlun, China earthquake. (b): Relative energy release as a function of time. (c): Location (distance from the epicenter) of the energy release in each time window. The circle and square respectively indicate the total energy release and energy value that is $\geq 50\%$ of the maximum amplitude in each time window.

The choice of a small earthquake as the reference event is important in this method, because final images of the energy radiation are largely controlled by the spatial image over time derived from the smaller reference event. To test how the choice of the reference event affects the final results, we carry out the inversion using a different reference event (14 April 2010, 01:25:17.8 M_w 6.1, 96.45E, 33.20N, depth 7.5 km) located 630 km southeast of the epicenter of the 2001 Kunlun earthquake. From the inversion, the locations of the sources of high frequency energy radiations show a similar pattern to the results obtained from the first reference event that is located closer to the mainshock epicenter, although there is some eastward offset probably due to the structural difference in the regions of the two reference earthquakes (Fig. S2). We also carry out the inversion using a point source that is used in the section of numerical test. The final pattern does not show large difference as compared to the other two, although there seems a systematical location shift, which is probably due to the complex

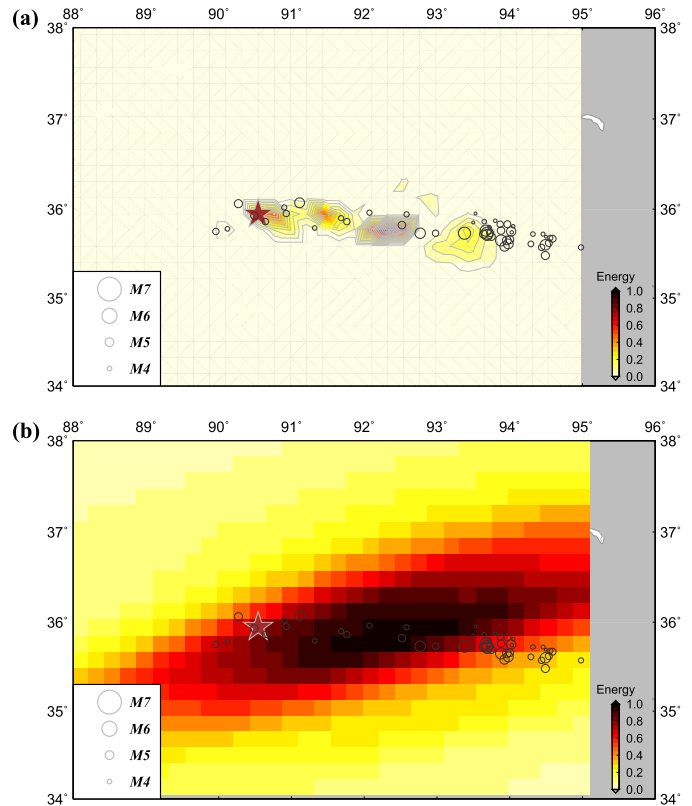


Fig. 8. Comparison of the total energy release of the 2001 M_w 7.8 Kunlun earthquake for our method (a) and the standard back-projection (b). Star indicates the epicenter (USGS). The circles represent the aftershocks three months following the mainshock.

structure in the source region and/or the location uncertainties for the two reference events (Fig. S2).

To further test how this method works for cases where seismograms of subevents are temporally overlapped, we perform another test using waveforms that are constructed by summing those of the mainshock and of the M_w 5.8 earthquake. The seismograms for the M_w 5.8 earthquake are 10 times amplified, to make them comparable in amplitude to the mainshock. Notice that the noises are also amplified. The time of the M_w 5.8 earthquake is set so that the initial arrival at the reference station (N.SYOH) is the same time as the initial arrival of the mainshock (Fig. S3a). We also tested for cases that the time is delayed by 20, 40, 60, and 80 s, respectively (Fig. S3b–e). For the inversion, we use the M_w 5.8 earthquake as a reference event. The rupture pattern of the mainshock and the location of M_w 5.8 earthquake are generally recovered for all of the tested cases, although there are some minor variations among them (Fig. S3). On the other hand, the time resolution appears to be largely affected, and we attribute this to the effect of the added amplified noise. If the M_w 6.1 earthquake (located 630 km away) is used as the reference event, as for the worst case scenario, the final rupture pattern for the mainshock varies. But the large asperity locations are generally consistent with each other (Fig. S4).

5. Discussion

We have demonstrated that the new method can provide images with improved spatial and temporal resolution of the source energy radiations using seismic array data that are recorded 30° to 90° from the epicenter. The direct P-wave is recorded clearly and is separated from other phases at this epicentral distance range, although it is not well separated from depth phases for a shallow

event. This method works best for the 2001 Kunlun earthquake because the steep dip of the fault plane naturally make this a 1D rupture in space. But for megathrust earthquakes, more reference events at different depths might be needed to account for the depth variations of large earthquakes. At epicentral distances of 10° to 30° , the P-waves are complicated by the triplication, and thus difficult to be used for the back-projection. Applying this approach should allow us to improve the temporal and spatial resolution of the back-projected images derived from regional data, and therefore is an interesting future work for obtaining faster source image in quasi-real time seismology.

There are basically two classes of approaches that are commonly employed to analyze earthquake rupture processes: the standard finite fault slip inversion approach (i.e. Kikuchi and Kanamori, 1991) and the adjoint approach, such as the time reversal (Larmat et al., 2006) or the back-projection (e.g., Ishii et al., 2005; Krüger and Ohrnberger, 2005). Using the line of argument originally provided by Claerbout and Black (2005), Kawakatsu and Montagner (2008) nicely illustrated that the difference may be noticed as that of “inversion and imaging”; while “inversion” solves for the inverse of the forward problem (e.g., $d = Gm$) via the inverse operator, G^{-1} , “imaging”, such as time reversal, solves for an approximate solution via the adjoint operator G^* . While inverse operators in geophysics are often ill-conditioned and unstable, adjoint operators are stable and provide robust approximate solutions.

The finite fault slip inversion may work well for modeling seismic waves in low frequency bands (say below 0.5 Hz), but in higher frequency bands, the Green's functions become complicated to be accurately modeled and the inversion becomes highly unstable and inapplicable. Our new method (Image Deconvolution Back Projection, IDBP) resolves this problem by first obtaining a robust back-projection adjoint image that will be secondly inverted (deconvolved) for source energy radiation. The second procedure (deconvolution of the array response) appears relatively stable, and therefore offers stable sharper image of the radiated energy for the high frequency waves. The IDBP method seems to work well, at least, for the strike-slip environments as demonstrated here, and its usefulness for other mechanism systems (thrust or normal faults) should be further investigated.

6. Conclusion

We have developed a novel approach for estimating high frequency energy radiations of seismic source by inversion based on images derived from back-projection. The synthetic test that uses the geometry of the 2001 M_w 7.8 Kunlun earthquake and station locations in Hi-net, shows that this new method can offer much sharper images of the radiated energy and rupture patterns compared to standard back-projection, since we correct for the array response in space and time. We estimated the high frequency energy radiations for the 2001 M_w 7.8 Kunlun earthquake using data recorded by Hi-net. Our results are generally similar to other studies using similar or different methods (Bouchon and Vallee, 2003; Lin et al., 2003; Antolik et al., 2004; Ozacar and Beck, 2004; Robinson et al., 2006; Vallée et al., 2008; Walker and Shearer, 2009), however, we are able to resolve much better details of the rupture propagation in high frequency range.

Acknowledgements

This work was supported by JSPS fellowship (P13324), NSFC grants 41004020 and 41474050 (D.W.). We thank the data services from the National Research Institute for Earth Science and Disaster Prevention data centers. Other data were obtained from the

USGS, and the GCMT websites. All the figures were created using the Generic Mapping Tools (Wessel and Smith, 1991).

Appendix A. Supplementary material

Supplementary material related to this article can be found online at <http://dx.doi.org/10.1016/j.epsl.2016.05.051>.

References

- Antolik, M., Abercrombie, R.E., Ekström, G., 2004. The 14 November 2001 Kokoxili (Kunlunshan), Tibet, earthquake: rupture transfer through a large extensional step-over. *Bull. Seismol. Soc. Am.* 94, 1173–1194.
- Bouchon, M., Vallee, M., 2003. Observation of long supershear rupture during the magnitude 8.1 Kunlunshan earthquake. *Science* 301, 824–826.
- Claerbout, J., Black, J., 2005. *Basic Earth Imaging*. Stanford University, pp. 11–22.
- D'Amico, S., Koper, K.D., Herrmann, R.B., Akinci, A., Malagnini, L., 2010. Imaging the rupture of the Mw 6.3 April 6, 2009 L'Aquila, Italy earthquake using back-projection of teleseismic P-waves. *Geophys. Res. Lett.* 37. <http://dx.doi.org/10.1029/2009GL042156>.
- Haney, M.M., 2014. Backprojection of volcanic tremor. *Geophys. Res. Lett.* 41, 1923–1928.
- He, X., Ni, S., Ye, L., Lay, T., Liu, Q., Koper, K.D., 2015. Rapid seismological quantification of source parameters of the 25 April 2015 Nepal earthquake. *Seismol. Res. Lett.* 86, 1568–1577.
- Honda, R., Yukutake, Y., Ito, H., Harada, M., Aketagawa, T., Yoshida, A., Sakai, S.i., Nakagawa, S., Hirata, N., Obara, K., 2011. A complex rupture image of the 2011 off the Pacific coast of Tohoku Earthquake revealed by the MeSO-net. *Earth Planets Space* 63, 583–588.
- Ishii, M., 2011. High-frequency rupture properties of the Mw 9.0 off the Pacific coast of Tohoku earthquake. *Earth Planets Space* 63, 609–614.
- Ishii, M., Shearer, P.M., Houston, H., Vidale, J.E., 2005. Extent, duration and speed of the 2004 Sumatra–Andaman earthquake imaged by the Hi-Net array. *Nature* 435, 933–936.
- Kawakatsu, H., Montagner, J.-P., 2008. Time-reversal seismic-source imaging and moment-tensor inversion. *Geophys. J. Int.* 175, 686–688.
- Kennett, B., Gorbatov, A., Spiliopoulos, S., 2014. Tracking high-frequency seismic source evolution: 2004 Mw 8.1 Macquarie event. *Geophys. Res. Lett.* 41, 1187–1193.
- Kikuchi, M., Kanamori, H., 1991. Inversion of complex body waves—III. *Bull. Seismol. Soc. Am.* 81, 2335–2350.
- Koper, K.D., Hutko, A.R., Lay, T., Sufri, O., 2012. Imaging short-period seismic radiation from the 27 February 2010 Chile (MW 8.8) earthquake by back-projection of P, PP, and PKIKP waves. *J. Geophys. Res. B, Solid Earth* 117. <http://dx.doi.org/10.1029/2011JB008576>.
- Krüger, F., Ohrnberger, M., 2005. Tracking the rupture of the M-w = 9.3 Sumatra earthquake over 1150 km at teleseismic distance. *Nature* 435, 937–939.
- Larmat, C., Montagner, J.P., Fink, M., Capdeville, Y., Tourin, A., Clévédy, E., 2006. Time-reversal imaging of seismic sources and application to the great Sumatra earthquake. *Geophys. Res. Lett.* 33. <http://dx.doi.org/10.1029/2006GL026336>.
- Laske, G., Masters, G., Reif, C., 2001. CRUST 2.0: a new global crustal model at 2×2 degrees. Institute of Geophysics and Planetary Physics, The University of California, San Diego. Website: <http://mahi.ucsd.edu/Gabi/rem.dir/crust2.html>.
- Lawson, C.L., Hanson, R.J., 1974. *Solving Least Squares Problems*. SIAM.
- Lay, T., Kanamori, H., Ammon, C.J., Hutko, A.R., Furlong, K., Rivera, L., 2009. The 2006–2007 Kuril Islands great earthquake sequence. *J. Geophys. Res. B, Solid Earth* 114. <http://dx.doi.org/10.1029/2008JB006280>.
- Lin, A., Kikuchi, M., Fu, B., 2003. Rupture segmentation and process of the 2001 Mw 7.8 central Kunlun, China, earthquake. *Bull. Seismol. Soc. Am.* 93, 2477–2492.
- Meng, L., Inbal, A., Ampuero, J.P., 2011. A window into the complexity of the dynamic rupture of the 2011 Mw 9 Tohoku–Oki earthquake. *Geophys. Res. Lett.* 38. <http://dx.doi.org/10.1029/2011GL048118>.
- Nakahara, H., Haney, M.M., 2015. Point spread functions for earthquake source imaging: an interpretation based on seismic interferometry. *Geophys. J. Int.* 202, 54–61.
- Okada, Y., Kasahara, K., Hori, S., Obara, K., Sekiguchi, S., Fujiwara, H., Yamamoto, A., 2004. Recent progress of seismic observation networks in Japan–Hi-net, F-net, K-NET and KiK-net. *Earth Planets Space* 56, xv–xxviii.
- Ozacar, A.A., Beck, S.L., 2004. The 2002 Denali fault and 2001 Kunlun fault earthquakes: complex rupture processes of two large strike-slip events. *Bull. Seismol. Soc. Am.* 94, S278–S292.
- Robinson, D., Brough, C., Das, S., 2006. The Mw 7.8, 2001 Kunlunshan earthquake: extreme rupture speed variability and effect of fault geometry. *J. Geophys. Res. B, Solid Earth* 111. <http://dx.doi.org/10.1029/2005JB004137>.
- Vallée, M., Landès, M., Shapiro, N., Klinger, Y., 2008. The 14 November 2001 Kokoxili (Tibet) earthquake: high-frequency seismic radiation originating from the transitions between sub-Rayleigh and supershear rupture velocity regimes. *J. Geophys. Res. B, Solid Earth* 113. <http://dx.doi.org/10.1029/2007JB005520>.

- Walker, K.T., Shearer, P.M., 2009. Illuminating the near-sonic rupture velocities of the intracontinental Kokoxili Mw 7.8 and Denali fault Mw 7.9 strike-slip earthquakes with global P wave back projection imaging. *J. Geophys. Res. B, Solid Earth* 114. <http://dx.doi.org/10.1029/2008JB005738>.
- Wang, D., Mori, J., 2011. Rupture process of the 2011 off the Pacific coast of Tohoku Earthquake (M (w) 9.0) as imaged with back-projection of teleseismic P-waves. *Earth Planets Space* 63, 603. <http://dx.doi.org/10.5047/eps.2011.05.029>.
- Wang, D., Mori, J., Koketsu, K., 2016. Fast rupture propagation for large strike-slip earthquakes. *Earth Planet. Sci. Lett.* 440, 115–126.
- Wang, D., Mori, J., Uchide, T., 2012. Supershear rupture on multiple faults for the M-w 8.6 Off Northern Sumatra, Indonesia earthquake of April 11, 2012. *Geophys. Res. Lett.* 39. <http://dx.doi.org/10.1029/2012GL053622>.
- Wessel, P., Smith, W.H., 1991. Free software helps map and display data. *Eos Trans. AGU* 72, 441–446.
- Xu, X., Yu, G., Klinger, Y., Tapponnier, P., Van Der Woerd, J., 2006. Reevaluation of surface rupture parameters and faulting segmentation of the 2001 Kunlunshan earthquake (Mw 7.8), northern Tibetan Plateau, China. *J. Geophys. Res. B, Solid Earth* 111. <http://dx.doi.org/10.1029/2004JB003488>.
- Xu, Y., Koper, K.D., Sufri, O., Zhu, L.P., Hutko, A.R., 2009. Rupture imaging of the M-w 7.9 12 May 2008 Wenchuan earthquake from back projection of teleseismic P waves. *Geochem. Geophys. Geosyst.* 10. <http://dx.doi.org/10.1029/2008GC002335>.
- Yagi, Y., Nakao, A., Kasahara, A., 2012. Smooth and rapid slip near the Japan Trench during the 2011 Tohoku-oki earthquake revealed by a hybrid back-projection method. *Earth Planet. Sci. Lett.* 355, 94–101.
- Yao, H., Shearer, P.M., Gerstoft, P., 2012. Subevent location and rupture imaging using iterative backprojection for the 2011 Tohoku Mw 9.0 earthquake. *Geophys. J. Int.* 190, 1152–1168.
- Yao, H., Shearer, P.M., Gerstoft, P., 2013. Compressive sensing of frequency-dependent seismic radiation from subduction zone megathrust ruptures. *Proc. Natl. Acad. Sci. USA* 110, 4512–4517.